In Situ Bragg Coherent Diffraction Imaging Study of a Cement Phase Microcrystal during Hydration

Xianping Liu,*[†,‡,●] Miguel A. G. Aranda,[§,‖] Bo Chen,[⊥,#,†] Peiming Wang,[†,‡] Ross Harder,[¶] and Ian Robinson*[⊥,#,†,●]

[†]School of Materials Science and Engineering and [‡]Key Laboratory of Advanced Civil Engineering Materials, Ministry of Education, Tongji University, Shanghai 201804, China

[§]Departamento de Química Inorgánica, Crystalografía y Mineralogía, Universidad de Málaga, 29071-Málaga, Spain

[‖]ALBA Synchrotron, Carretera BP 1413, Km. 3.3, E-08290 Cerdanyola, Barcelona, Spain

[⊥]London Centre for Nanotechnology, University College London, London WC1H 0AH, United Kingdom

[#]Research Complex at Harwell, Rutherford Appleton Laboratory, Oxfordshire OX11 0FA, United Kingdom

[¶]Advanced Photon Source, Argonne National Laboratory, Argonne, Illinois 60439, United States

S Supporting Information

ABSTRACT: Results of Bragg coherent diffraction imaging (BCDI) confirm that ion migration and consumption occur during hydration of calcium monoaluminate (CA). The chemical phase transformation promotes the hydration process and the formation of new hydrates. There is a potential for the formation of hydrates near where the active ions accumulate. BCDI has been used to study the in situ hydration process of CA over a 3 day period. The evolution of three-dimensional (3D) Bragg diffraction electron density, the "Bragg density", and strain fields present on the nanoscale within the crystal

was measured and visualized. Initial Bragg densities and strains in CA crystal derived from sintering evolve into various degrees during hydration. The variation of Bragg density within the crystal is attributed to the change of the degree of crystal ordering, which could occur through ion transfer during hydration. The observed strain, coming from the interfacial mismatch effect between high Bragg density and low Bragg density parts in the crystal, remained throughout the experiment. The first Bragg density change during the hydration process is due to a big loss of Bragg density as seen in the image amplitude but not its phase. This work provides new evidence supporting the through-solution reaction mechanism of CA.
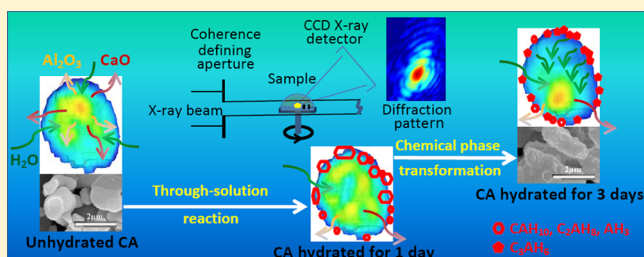
Calcium monoaluminate, $CaAl_2O_4$ (CA in cement nomenclature) is the main active mineralogical component of calcium aluminate cements (CACs). These cements are mainly used in the applications at high temperature, such as refractory bricks, and also for winter construction work.[1] CA crystallizes in a monoclinic crystal structure through solid-state reaction between CaO and Al_2O_3[2,3] by sintering. This cement constituent was selected for study because of its fast hydration kinetics (faster than the main constituent of Portland cements, tricalcium silicate, C_3S). CA can be prepared with clean flat facets, and it can serve as a model for cement hydration.

The hydration mechanism of CA is well-known as through-solution reaction using various analysis technologies.[4−6] The CA hydration process arises by dissolution in water of reactants and the achievement of saturated solution. Subsequently, the crystallization of calcium aluminate hydrates occurs; as a final process, the hydrate crystallization is highly temperature dependent.[7] At temperatures below 10 °C, the formation of hexagonal CAH_{10} (C = CaO, A = Al_2O_3, H = H_2O) is favored by reaction .

$$CA + 10H \rightarrow CAH_{10} \tag{1}$$

Once above 10 °C, the formation of another hexagonal calcium aluminate hydrate[8] (C_2AH_8) with AH_3 may occur through the reaction 2, jointly with reaction 1. AH_3 is initially an amorphous hydrated aluminum oxide gel that later may crystallize as hexagonal gibbsite.

$$2CA + 11H \rightarrow C_2AH_8 + AH_3 \tag{2}$$

These hydrates (CAH_{10} and C_2AH_8) are metastable and tend to convert to the thermodynamically stable calcium aluminate hydrate,[9] C_3AH_6, which has a hydrogarnet structure type, i.e., cubic structure, according to reactions 3 and 4.

$$3CAH_{10} \rightarrow C_3AH_6 + 2AH_3 + 18H \tag{3}$$

$$3C_2AH_8 \rightarrow 2C_3AH_6 + AH_3 + 9H \tag{4}$$
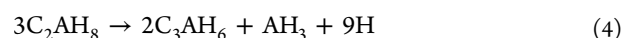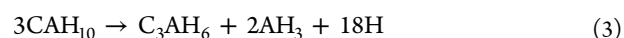
At higher temperatures, above 70 °C, the formation of C_3AH_6 and AH_3 follows reaction 5.[10]

$$3CA + 12H \rightarrow C_3AH_6 + 2AH_3 \qquad (5)$$

However, due to properties of the highly temperature dependent hydration of CA, the hydration process may also comprise chemical reactions with different hydration mechanisms. For example, at temperatures ranging from 60 to 90 °C, the solid-state reaction mechanism was reported using synchrotron energy-dispersive diffraction resulting layers of hydrates.[11] Similar observations were found at other temperatures.[12,13]

There is a dispute between the through-solution reaction mechanism and the solid-state reaction mechanism, because it is difficult to give a definite explanation to some phenomena with a single mechanism due to the limitation of the available characterization methods. According to the through-solution reaction mechanism, due to the enormous and fast early dissolution of CA, a compact layer of hydrates formed surrounding unreacted CA crystals, precipitating in air-filled porosity homogeneously and not far away from the surface of CA crystals. CaO has a higher solubility than Al_2O_3, therefore the surface of CA became rich in Al_2O_3 after 20 min of hydration.[14] The composition of pore solution also changed by precipitation of noncrystalline hydrates.[9] However, according to the solid-state reaction mechanism, an initial film barrier of the hydrates was formed on the surface of the unhydrated crystals, which prevents water molecules from reaching the unreacted CA surface.[15,16] Both hydration mechanisms lead to the slowly decreasing hydration rate, after the main reaction period, due to a diffusion controlled process. The diffusion species in the former mechanism are the dissolved ions from CA, and for the latter mechanism the water.[9,11] Further hydration of CA was hindered after fast early hydration.[12,17]

The understanding of the hydration mechanism of CA will help to establish a reliable hydration mechanism of the more complicated calcium aluminate cement systems. Hence it is the central issue surrounding the application of cement to achieve a higher level of performance. Although a great deal of the hydration mechanism of CA is already understood, they have been confined by either the static or indirect instinct of the characterization methods, which is not comprehensive under the current technical conditions.

The structural origin of reactivity of the cement clinker can be addressed by visualizing evolution of the crystal structure of its minerals during hydration. Transmission electron microscopy (TEM) can be used to investigate defects at near-atomic-scale resolution or characterize defect dynamics in real time.[18] However, the requirements for electronically transparent samples make the samples themselves usually not representative of the bulk material. In addition, the required vacuum is not compatible with hydrating conditions. Alternatively, the X-ray method to probe materials with 3D images[19,20] or crystal structures has improved to achieve spatial resolution approaching 10 nm.[21] Bragg coherent diffraction imaging (BCDI) not only is such a powerful new method to obtain three-dimensional (3D) images of individual crystals on the nanoscale through inversion of the diffraction data by computational method, but it is also highly sensitive to crystal defects and strain fields inside crystals seen as phase evolution.[21−24] The phase measures the projection of the lattice distortion onto the direction of the measured Bragg

peak. Additionally, the experimental conditions are compatible with in situ cement hydration characterization.

In this Communication, we concentrate on the application of BCDI for investigating in situ 3D Bragg diffraction electron density ("Bragg density") and strain evolution of a CA microcrystal during 3 days of hydration. Bragg diffraction patterns were used to select an individual CA crystal and characterize the evolution of the crystalline parts of it. The density seen upon inversion of the BCDI data at a given Bragg peak encompasses both the physical electron density and the degree of crystalline order. This is not the same as physical density because it includes all the crystal properties that affect the strength of a Bragg peak, such as crystal defects (planar faulting, dislocations, and point defects), thermal disorder, and so forth. Bragg density is also diminished whenever the crystal undergoes phase transformations and begins to adopt a secondary crystal structure. The strain field distribution is also imaged by BCDI[16] and its evolution during hydration was recorded accordingly. Through the Bragg density and strain, we expected to find new evidence for the CA hydration mechanism.

CA was prepared by high temperature synthesis using the appropriate stoichiometric mixtures of $CaCO_3$ and Al_2O_3, with a grinding process taking place between each heating step (see the Supporting Information S1). The sample was measured with scanning electron microscopy (SEM) and laboratory X-ray powder diffractometry (XRPD). The size of the CA crystals was about 1 μm (Figure S1a). The synthesized sample was confirmed to contain 94.9(1) wt % of monoclinic CA (see the Supporting Information S2). Some of the CA was ground into microcrystals and spread on a clean silicon wafer substrate, and then heated in an oven at 500 °C for half an hour to be attached on the silicon wafer for coherent diffraction data collection. Then, the silicon wafer together with the sample was wrapped with Kapton film to form an open chamber. After data collection of a selected unhydrated CA crystal, saturated potassium sulfate solution was injected into a container inside the chamber. The chamber was then sealed with the sticky side of the Kapton film to get a relative humidity of 98% at 20 °C inside the Kapton bag (Figure 1). The CA microcrystal began to hydrate when it came into contact with the water vapor, and data collection of the same CA crystal as that before hydration was performed subsequently at different time intervals. After
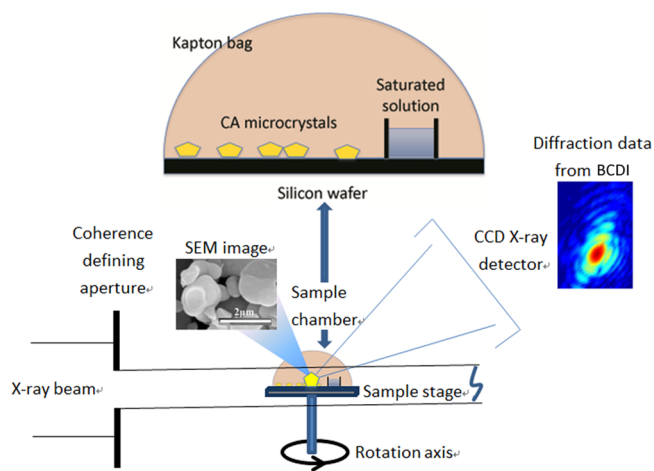

Figure 1. Schematic sample chamber and experiment setup at the beamline 34-ID-C at APS.

the experiment was finished, the silicon wafers, containing partially hydrated crystals, were removed from the bag, sealed, and later studied by SEM.

The BCDI measurement was made at the beamline 34-ID-C at the Advanced Photon Source (APS). The schematic experimental setup is illustrated in Figure 1. Samples were mounted on kinematic mounts with a reproducibility position accuracy of 1−2 μm. With the aid of a confocal microscope, the same crystal can be measured repeatedly over a long period of time. The coherent monochromatic X-ray beam (9 keV) was defined by passing through an entrance slit of 60(v) × 30(h) microns, then focused by the Kirkpatrick-Baez (KB) mirrors to a size of approximately 1 μm. Initially, the diffraction peaks were located by a 2D Pilatus detector, then the diffraction from the sample was collected by a charge-coupled device (CCD) detector located 1 m away. 3D data were acquired as stacks of 2D CCD frames collected over rocking curves[16] of the principal sample rotation axis, perpendicular to the X-ray beam. A typical scan spans a 0.4° range (which may slightly depend upon the width of the recorded signal for the reflection) with a rocking angle of 0.005° which resulted in 80 frames. Each frame was recorded for 2 s, and to improve the statistical accuracy, 15 acquisitions were taken. Therefore, it took 40 min to collect one full set of 3D data.

These 3D diffraction patterns were inverted to 3D images using Fienup's Hybrid Input−Output algorithm[25] to phase retrieve the diffraction patterns.[24] The "support" function describing the crystal shape was derived by using a "shrink-wrap" procedure[26] from the initial data set and fixed for the time-evolved images. The final images were transformed to Cartesian laboratory coordinates for viewing.[24] Results showing isosurface view (Figure 2) and cross-sectional views (Figure 3
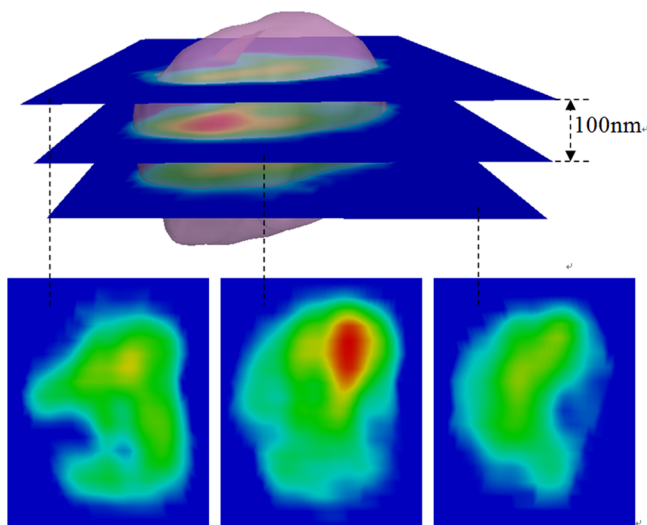

Figure 2. 50% translucent isosurface view of the outer surface of the imaged crystal showing three slices of the unhydrated crystal. The middle slice, which captures most of the 3D information, is used to monitor the hydration.

and Figure 4) of the imaged crystal, which visualize the outer surface and the interior of the crystal, are presented in this report. The spatial resolution of the resulting 3D images is approximately 30 nm.[16] The densities of the CA crystal were detected by the amplitude of this Bragg density function (Figure 3), which was interpreted as the degree of crystal ordering coupled with the Bragg peak. Strains were detected as
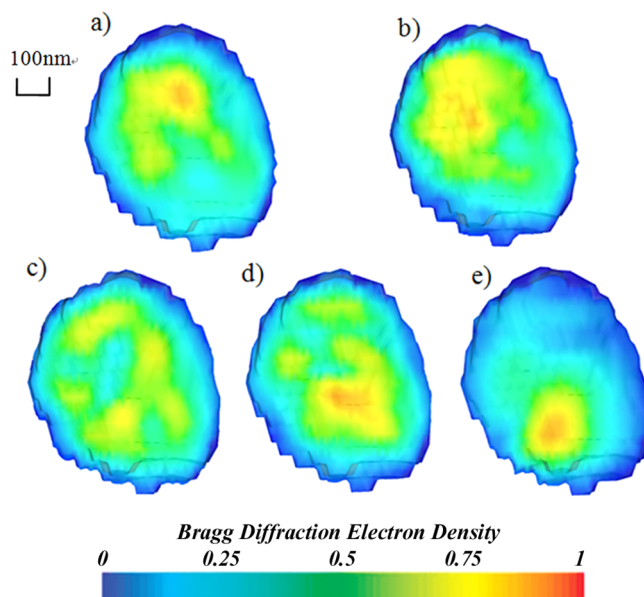

Figure 3. Cross sections through the reconstructed 3D images of the CA crystal showing the internal Bragg density variations during 3 days of hydration measured by BCDI: (a) unhydrated CA, (b) CA hydrated for 2 h, (c) CA hydrated for 24 h, (d) CA hydrated for 52 h, (e) CA hydrated for 67 h.
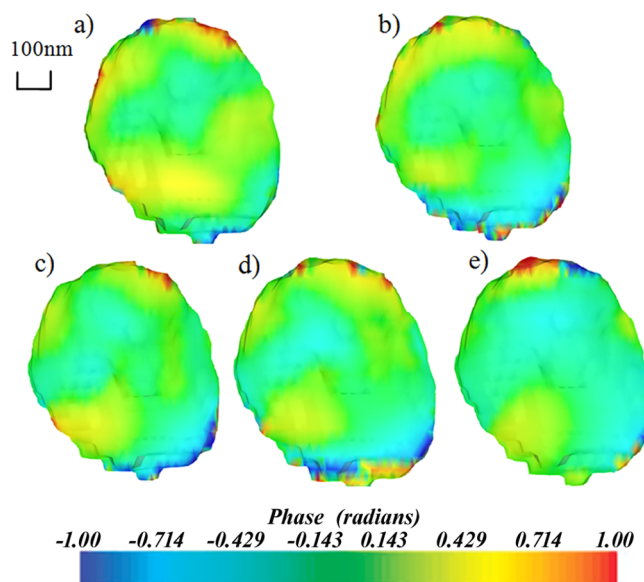

Figure 4. Corresponding maps showing the phase of the same cross sections as in Figure 3: (a) unhydrated CA, (b) CA hydrated for 2 h, (c) CA hydrated for 24 h, (d) CA hydrated for 52 h, (e) CA hydrated for 67 h.

phase in the real-space images (Figure 4), which was interpreted as the projection of a 3D deformation field arising from sintering, interfacial contact forces between the crystals, interfacial mismatching effect between high Bragg density and low Bragg density parts, as well as from the dissolution force of etch pit on the crystal surface.

Figure 2 shows translucent isosurface view of the reconstructed 3D image of the unhydrated CA crystal during hydration with three of its cut-through sections rendered in color. The 20% isosurface dimensions of the crystal are Δx = 490 nm, Δy = 545 nm, and Δz = 665 nm. The reconstructed

3D images of the crystal with time evolution in Figure 3 and Figure 4 are shown in just the middle section, since they capture most of the 3D information during the hydration and can well represent the crystal as Figure 2 shows.

Figure 3 shows the middle cross sections through the reconstructed 3D images of the Bragg density of a single CA microcrystal during 3 days of hydration. The Bragg density is color-coded from dark blue to red (from 0 to 1); all the images are on the same scale. The Bragg density values are all relative within each image. However, the maximum does not vary much from one time to the next. As explained above, higher values of Bragg density correspond to higher degrees of crystal ordering. In most cases, the high Bragg density areas are surrounded with gradually lower Bragg density areas in the crystal, which indicates there is a high crystal ordering center in the crystal. The periphery of the cross section is of the lowest Bragg density since the crystal dissolution starts from the surface.

It can be hypothesized that if the hydration is controlled by the through-solution reaction mechanism, the CaO and Al_2O_3 ions originally present in the CA crystalline lattice diffuse from the interior to the surface following water permeation, causing variation of Bragg density gradient or crystallization gradient in the crystal. Hydrate precipitates when liquid constituent becomes oversaturated at the CA surface, whereas if the hydration is controlled by the solid-state reaction mechanism, the distribution of the Bragg density or crystallization will not change since only water diffuses through the initial hydrate barrier.

When comparing the Bragg density distribution of unhydrated CA crystal (Figure 3a) originating from sintering, with the crystal after 2−24 h hydration, the higher Bragg density area (orange area) totally transformed into relatively low Bragg density area (yellow area) and the low Bragg density area (yellow area) was surrounded with the lower Bragg density areas (green and blue areas) enlarged toward the surface (Figure 3b and c), which indicated the decrease of the degree of crystal ordering inside the crystal with the transfer of CaO and Al_2O_3 ions from the crystalline lattice. After 52 h and almost 3 days of hydration (Figure 3d and e), the higher Bragg density areas (orange area) gradually appeared again in another area of the crystal, with increased dark blue areas at the right side. According to reactions 3 and 4, hexagonal CAH_{10} and C_2AH_8 may convert to the thermodynamically stable cubic C_3AH_6 and release water molecules during hydration at 20 °C. The released water increased the local water to binder ratio, then further benefited the local ion migration to the adjacent area, hence reducing the Bragg density and the degree of crystal ordering near the edge at right (dark blue area at right side in Figure 3e). However, it increased the degree of crystal ordering on the opposite side (orange area in Figure 3d and e). The reappearance of a higher Bragg density area elsewhere benefited the formation of saturated solution nearby, therefore accelerating the crystallization of calcium aluminate hydrates on a new site. From the SEM images of the hydrated CA for 3 days (Figure S1b), there were homogeneously distributed nanoscale hydrogarnets on the surface of CA. This revealed that the hydration took place and hydrates precipitated on different sites within 3 days of hydration. Thus, the through-solution reaction mechanism was confirmed.

Figure 4 shows the reconstructed 3D images of the phase within the single CA crystal as a function of time during 3 days of hydration. It is coded in color from dark blue to red (from −1.00 to 1.00 rad). All images are on the same scale, but the

phase values are all relative within each image, and can only be compared within each image; there is an arbitrary offset between images. Positive value indicates tensile strain and negative value indicates compressive strain. The higher the value, the higher the strain is. There are three levels of strain in the crystal: positive, zero, and negative. Positive and negative areas mixed up in the unhydrated CA crystal with transition zero value region, which we consider to represent the initial pattern of compressive and tensile strains originating from sintering (Figure 4a). Part of the initial pattern of strains observed in the crystal comes from interfacial mismatching effect between high Bragg density and low Bragg density parts, which remains throughout 3 days of hydration. The contact force between deposited hydrates and unhydrated crystals on the surface is considered to be directly proportional to the negative surface strain field. Although the strain effects are very subtle during 3 days of hydration, the negative area on the periphery of the cross section of the crystal enlarged at 3 days (Figure 4e). When Figure 3e and Figure 4e were compared accordingly, it was found that the newly formed low Bragg density area was almost at the same location as the newly formed negative phase area. This means that there is a potential for the formation of hydrates near where the active ions accumulate, and the chemical phase transformation promotes the expansion of low Bragg density area and the formation of new high Bragg density area, which helped the hydration process and the formation of new hydrates. Thus, the through-solution reaction mechanism was also confirmed by phase images.

According to defect-generated dissolution theories, the bulk dissolution rate of crystals is explained by the dissolution step waves originating from etch pits on the surface.[27] Due to the strain field of a dislocation, the hollow core is opened up and an etch pit is formed for a system far from equilibrium conditions,[17,28] resulting in consistent global dissolution throughout the surface of the crystal.[27] Therefore, the dissolution force of an etch pit on the crystal surface is considered to be directly proportional to the positive surface strain field. However, there is no evidence for the surface strain field from etch pits during crystal dissolution. The possible reason is that the system is not far from equilibrium conditions.

From the analysis of the CA hydration measured by BCDI in this work, we can draw the following conclusions.

1. A through-solution reaction (homogenized crystallization) mechanism during the hydration of CA was confirmed with BCDI, but defect-generated dissolution theory was not supported.

2. Initial Bragg densities and strains in CA crystal were derived from sintering. The degree of crystal ordering decreased due to ion transfer during hydration. The strain coming from the interfacial mismatch effect between high Bragg density and low Bragg density parts in the crystal remained throughout the experiment.

3. The chemical phase transformation promoted the hydration process and the formation of new hydrates.

4. The first change of Bragg density during the hydration process was due to a big loss of Bragg density as seen in the image amplitude but not its phase.

■ ASSOCIATED CONTENT

ⓢ Supporting Information

$CaAl_2O_4$ synthetic procedure details. Basic characterization of $CaAl_2O_4$ by SEM (anhydrous and hydrated) and Rietveld

quantitative phase analysis using laboratory X-ray powder diffractometer (anhydrous). The Supporting Information is available free of charge on the ACS Publications website at DOI: 10.1021/cg5013389.

■ AUTHOR INFORMATION

Corresponding Authors
*E-mail: lxp@tongji.edu.cn.
*E-mail: i.robinson@ucl.ac.uk.

Author Contributions
●Xianping Liu and Ian Robinson contributed equally.

Notes
The authors declare no competing financial interest.

■ ACKNOWLEDGMENTS

■ REFERENCES

(1) Bensted, J. In *Structure and Performances of Cements*, 2nd ed.; Bensted, J., Barnes, P., Eds.; Spon Press: London, 2002; Chapter 4, p 114.

(2) Rivas Mercury, J. M.; De Aza, A. H.; Pena, P. *J. Eur. Ceram. Soc.* **2005**, *25*, 3269−3279.

(3) Goodwin, D. W.; Lindop, A. J. *Acta Crystallogr., Sect. B* **1970**, *26*, 1230−1235.

(4) Cottin, B. *Cem. Concr. Res.* **1971**, *1*, 273−284.

(5) Torréns-Martín, D.; Fernández-Carrasco, L.; Martínez-Ramírez, S. *Cem. Concr. Res.* **2013**, *47*, 43−50.

(6) Lamour, V. H. R.; Monteiro, P. J. M.; Scrivener, K. L.; Fryda, H. *Microscopic studies of the early hydration of calcium aluminate cements*; International Conference on Calcium Aluminate cement (CAC); Edinburgh, UK; July 2001; pp 169−180.

(7) Scrivener, K. L.; Capmas, A. In *Leás Chemistry of Cement and Concrete*, 4th ed.; Hewlett, P. C., Ed.; Arnold: London, 1998; Chapter 13, pp 723−727.

(8) Jensen, T. R.; Christensen, A. N.; Hanson, J. C. *Cem. Concr. Res.* **2005**, *35*, 2300−2309.

(9) Klaus, S. R.; Neubauer, J.; Goetz-Neunhoeffer, F. *Cem. Concr. Res.* **2013**, *43*, 63−69.

(10) Scrivener, K. L.; Cabiron, J. L.; Letourneux, R. *Cem. Concr. Res.* **1999**, *29*, 1215−1223.

(11) Rashid, S.; Turrillas, X. *Thermochim. Acta* **1997**, *302*, 25−34.

(12) Geβner, W.; Trettin, R.; Rettel, A.; Müller, D. In *Calcium Aluminate Cements*; Mangabhai, R. J., Ed.; E and FN Spon: London, 1990; Chapter 8, pp 96.

(13) Bushnell-Watson, S. M.; Sharp, J. H. *Cem. Concr. Res.* **1990**, *20*, 677−686.

(14) Moehmel, S. *Freiberg Forschungsh. A* **2003**, *869*, 1−238.

(15) Fujii, K.; Kondo, W.; Ueno, H. *J. Am. Ceram. Soc.* **1986**, *69*, 361−364.

(16) Robinson, I.; Harder, R. *Nat. Mater.* **2009**, *8*, 291−298.

(17) Frank, F. C. *Acta Crystallogr.* **1951**, *4*, 497−501.

(18) Lee, T. C.; Robertson, I. M.; Birnbaum, H. K. *Philos. Mag. A* **1990**, *62*, 131−153.

(19) Chen, B.; Guizar-Sicairos, M.; Xiong, G.; Shemilt, L.; Diaz, A.; Nutter, J.; Burdet, N.; Huo, S.; Mancuso, J.; Monteith, A.; Vergeer, F.; Burgess, A.; Robinson, I. *Sci. Rep.* **2013**, *3*, 1177.

(20) Holler, M.; Diaz, A.; Guizar-Sicairos, M.; Karvinen, P.; Färm, E.; Härkönen, E.; Ritala, M.; Menzel, A.; Raabe, J.; Bunk, O. *Sci. Rep.* **2014**, *4*, 3857.

(21) Abbey, B. *JOM* **2013**, *65*, 1183−1201.

(22) Pfeifer, M. A.; Williams, G. J.; Vartanyants, I. A.; Harder, R.; Robinson, I. K. *Nature* **2006**, *442*, 63−66.

(23) Aranda, M. A. G.; Berenguer, F.; Bean, R. J.; Shi, X. W.; Xiong, G.; Collins, S. P.; Nave, C.; Robinson, I. K. *J. Synchrotron Radiat.* **2010**, *17*, 751−760.

(24) Harder, R.; Robinson, I. K. *JOM* **2013**, *65*, 1202−1207.

(25) Fienup, J. R. *Appl. Opt.* **1982**, *21*, 2758−2769.

(26) Marchesini, S.; He, H.; Chapman, H. N.; Hau-Riege, S. P.; Noy, A.; Howells, M. R.; Weierstall, U.; Spence, J. C. H. *Phys. Rev. B* **2003**, *68*, 140101.

(27) Lasaga, A. C.; Luttge, A. *Science* **2001**, *291*, 2400−2404.

(28) Cabrera, N.; Levine, M. M.; Plaskett, J. S. *Phys. Rev.* **1954**, *96*, 1153.